Reconstruction of the Three-Dimensional Structure of Simian Virus 40 and Visualization of the Chromatin Core

Timothy S. Baker; Jacqueline Drak; Minou Bina

Proceedings of the National Academy of Sciences of the United States of America, Vol. 85, No. 2 (Jan. 15, 1988), 422-426.

Proc. Natl. Acad. Sci. USA
Vol. 85, pp. 422–426, January 1988
Biophysics

Reconstruction of the three-dimensional structure of simian virus 40 and visualization of the chromatin core

(cryoelectron microscopy/image analysis/nucleosome/minichromosome/papovaviruses)

TIMOTHY S. BAKER*†, JACQUELINE DRAK‡§, AND MINOU BINA‡

Departments of *Biological Sciences and ‡Chemistry, Purdue University, West Lafayette, IN 47907

Communicated by Michael G. Rossmann, September 14, 1987 (received for review July 27, 1987)

ABSTRACT **The three-dimensional structure of the capsid and the nucleohistone core of simian virus 40 (SV40) has been reconstructed by image analysis of electron micrographs of frozen hydrated samples. The 72 prominent capsomere units that comprise the $T = 7d$ icosahedral surface lattice of the capsid are clearly resolved. Both the pentavalent and hexavalent capsomeres appear with pentameric substructure, indicating that bonding specificity in the shell is not quasi-equivalent. There is a remarkable similarity between the structure of the SV40 virion capsid and the structure reported for the polyoma empty capsid. This result establishes that (*i*) the unexpected pentameric substructure of the hexavalent capsomeres is also present in virions and (*ii*) the arrangement of the 72 pentamers in the capsid lattice may be a characteristic feature of the entire papova family of viruses. The center of the SV40 reconstruction reveals electron density corresponding to the nucleohistone core. This density is smeared, suggesting that the minichromosome is not organized with icosahedral symmetry matching the capsid symmetry. The visualization of the virion chromatin provides a basis for invoking new models for the higher order structure of the encapsidated minichromosome.**

Mature simian virus 40 (SV40) virions contain only proteins and DNA. The capsid encloses a minichromosome, which consists of the viral DNA folded into nucleosomes by the cellular core histones. Virion proteins VP1, VP2, and VP3 are involved in packaging the minichromosome into higher order structures and in forming the icosahedral capsid that surrounds the minichromosome (reviewed in refs. 1 and 2). The papovavirus B genus, to which SV40 belongs, includes polyoma, found in a large fraction of both wild and laboratory mice, and JC- and BK-type viruses, isolated from the brain tissues of certain patients with progressive multifocal leukoencephalopathy (reviewed in ref. 3).

The SV40 capsid examined by electron microscopy displays a characteristic morphology consisting of 12 five-coordinated (pentavalent) and 60 six-coordinated (hexavalent) capsomere units arranged on a right-handed $T = 7d$ icosahedral lattice (4–6). By using an approach in which single crystal x-ray diffraction intensities were phased from computed models, Rayment *et al.* (7) made the unexpected discovery that both the hexavalent and pentavalent morphological units of the polyoma empty capsid (capsid that does not contain DNA) consist of VP1 pentamers, indicating that the protein subunits in the polyoma capsid are not arranged according to predictions consistent with the quasi-equivalence theory (8). Baker *et al.* (9) subsequently established that the polymorphic tube aggregates found in polyoma-infected cells are also composed only of pentameric subunits. More recently, Salunke *et al.* (10) have discovered that a genetically engineered polyoma VP1, expressed in *Escherichia coli*, spontaneously associates to form pentamers, which polymerize under appropriate *in vitro* conditions to form spherical particles, whose structure resembles the empty capsid structure determined by Rayment *et al.* (7).

The unexpected discoveries presented have led to many intriguing questions: Are the hexavalent pentamers also present in the capsid of "full" virions? How does the bonding specificity of VP1 arise such that identical polypeptide chains fit into symmetrically distinct environments? Why do nonequivalently related subunits assemble into a structure with icosahedral symmetry? Is the structure observed for polyoma shared by other members of the papovavirus family? Does the structure of the minichromosome enclosed in the capsid conform to the icosahedral symmetry of the capsid?

To begin answering these questions, we have examined the structure of SV40 virions using cryoelectron microscopy (11–17). This technique circumvents some of the artifacts traditionally associated with negative-staining procedures. We followed Fourier image analysis procedures (18–21) to reconstruct the virion structure and to visualize the chromatin core found inside the capsid.

MATERIALS AND METHODS

Cells, Virus, and Infection. Virions were isolated from *wt776*-infected cells by implementing the following changes in published procedures (22, 23). To improve virion yield, we used the MA134 cell line (obtained from L. M. Hallick, Oregon Health Sciences University). The infected cells were harvested 8–10 days after infection, when cell lysis occurred. After removing the cellular debris and chromatin from the lysate (23), polyethylene glycol was added slowly to the supernatant, to a final concentration of 10%. Salt was not added to the supernatant to prevent virion dissociation and to minimize the production of empty capsids. The virions precipitated by polyethylene glycol were further purified by following CsCl banding procedures (23).

Sample Preparation and Electron Microscopy. Aqueous samples (3–4 μl) of SV40 virions (≈4 mg/ml in 12.5 mM Tris buffer at pH 7.4) were applied to holey carbon-coated electron microscope grids (made hydrophilic by glow discharge in an atmosphere of amyl amine), blotted with filter paper for a few seconds, and rapidly plunged into liquid ethane (14, 15). Grids were transferred under liquid nitrogen to a Gatan cold holder. The holder was inserted in a Philips EM400 electron microscope and maintained at about −165°C. The micrographs were recorded on Kodak SO-163 films using low-irradiation conditions (≈1000 e^-/nm^2 at the specimen). At

The publication costs of this article were defrayed in part by page charge payment. This article must therefore be hereby marked "*advertisement*" in accordance with 18 U.S.C. §1734 solely to indicate this fact.

Abbreviations: SV40, simian virus 40; VP1, -2, and -3, virion proteins 1, 2, and 3.

†To whom reprint requests should be addressed.
§Present address: Department of Chemistry, Yale University, New Haven, CT 06511.

doses >2000 e^-/nm^2, the virus particles suffer rapid irreversible damage. The characteristic capsomere morphology becomes smeared or disappears after a dose of ≈4000 e^-/nm^2. Bubbles form in the supporting ice layer and within the particles after 6000–8000 e^-/nm^2. The microscope was operated at 100 kV at a nominal magnification of ×33,000. The actual magnification (×27,400) was measured using the 49.5 nm diameter of polyomavirus (7) as an external standard (N. Olson, T.S.B., and J.D., unpublished results).

Several criteria aided our selection of the micrograph used for image analysis. We did not use micrographs that showed obvious specimen drift or vibration resulting mainly from instabilities in the microscope cold stage. The presence of residual image astigmatism or nonoptimum focusing of the microscope objective lens was identified in the remaining micrographs by optical or computer diffraction methods (21).

The micrograph selected for computing the three-dimensional reconstructions was recorded with the objective lens underfocused by 1–2 μm, a level of defocus at which the phase-contrast transfer function (CTF) of the microscope remains positive for all spatial frequencies within the 3.8 nm resolution limit of the reconstructions (24). Corrections for nonlinearities of the CTF (25) were not made since they did not significantly alter the subsequent reconstructions.

Image Analysis and Three-Dimensional Reconstruction. A region of the selected micrograph contained >100 virus particle images. This region was digitized at regular intervals (25 μm), corresponding to ≈0.92 nm at the specimen, and displayed on a raster graphics TV screen (Lexidata model 3400). Individual particles, randomly selected from this digitized image, were masked from their surroundings with circular boundaries. Images of virions that appeared distorted (nonspherical), degraded, empty, or touching or superimposed with neighboring particles were not included in the reconstructions. The selected particles displayed circular outlines, indicating that the spherical shape and icosahedral symmetry were well preserved.

After floating (26) and Fourier transforming selected particle images, the center of each particle was initially located to within a half raster step using a cross-correlation procedure, which identifies the centrosymmetric origin of an image. The parameters defining the view orientation and center (origin of symmetry axes) for each particle are interdependent. The original common lines method (20) was modified to allow these parameters to be refined to a unique solution in a few cycles of an iterative procedure (ref. 27; T.S.B. and J.D., unpublished data).

In the original procedure (20), the particle Fourier transform is searched for the positions of the best sets of common lines: pairs of lines along which, because of the symmetry of the particle, the transform should be the same. Since the relative distribution and number of unique pairs of common lines varies for different view parameters Θ, Φ, Ω (28), residuals measured along sets of common lines corresponding to different views are not strictly comparable. A weighting scheme was introduced in which, for every pair Θ, Φ, the residual is measured and then a χ^2 value is calculated. The probability of obtaining that χ^2 value is estimated by using (*i*) the matrix of residuals for a fixed Θ, Φ (with varying Ω) and (*ii*) the number of degrees of freedom. This number is calculated from the total number of points, for which residuals are evaluated (for a given Θ and Φ), and the actual number of common lines used. Each residual is subsequently multiplied by the reciprocal of the probability value. This provides a basis for distinguishing the various orientations that have similar unweighted residuals. It also identifies orientations that give false minima.

The final set of 30 particles selected represents the best images as judged by minimum common residuals. The view parameters of the particles differ sufficiently such that, together with icosahedral symmetry, the complete three-dimensional transform of the specimen could be evaluated by interpolation to spatial frequencies of 3–4 nm. We subsequently chose one particle image as reference and scaled the set of images to the same magnification and contrast. We combined the scaled data, by taking into account the relative orientations of the particles, to produce a three-dimensional Fourier transform.

Electron-density maps were computed by inverse Fourier–Bessel transformation of the three-dimensional transform, to 3.8 nm resolution, after constraining it to obey D_5 symmetry (20). The minimum common residuals for the particle images provided a basis for establishing the resolution limit of the reconstruction. The maps are displayed with the right-handed enantiomorph of the T = 7 skew lattice, consistent with the earlier hand determination (4). Computations were performed on a VAX11/750 minicomputer (Digital Equipment, Maynard, MA) using Fortran programs.

RESULTS AND DISCUSSION

Electron Microscopy, Image Analysis, and Three-Dimensional Reconstruction. Cryomicroscopy provides excellent preservation of the native morphology of the virus particles when compared with traditional staining procedures that usually lead to severe particle flattening, presumably because of surface tension effects present during dehydration of the samples. When embedded in thin layers of vitreous ice, most of the SV40 particles display circular image profiles, indicating that the spherical particle shape is well preserved by the preparative technique (Fig. 1). The best images are obtained from samples in which the thickness of the supporting vitreous ice layer is at least as large as the outside diameter of the virus particles (≈50 nm). Frozen hydrated SV40 specimens display relatively low contrast (low signal/noise ratio) compared to negatively stained samples. Nevertheless, since the capsomere is the dominant low-resolution feature of the capsid structure, the characteristic capsomere morphology is readily observed in the unstained samples when the images are strongly underfocused by 1–5 μm to enhance phase contrast (Fig. 1).

We computed three separate three-dimensional reconstructions by modifying procedures previously developed for analyzing negatively stained icosahedral particles (18–20). Two reconstructions were computed with independent sets of 15 particles; a third was computed by combining the entire set of 30 particles. The number of the particles used in our study exceeds the number typically required (usually 3–5) for computing the three-dimensional reconstruction of negatively stained icosahedral particles (18, 31–36). This is because the unstained particle images are much noisier and lower in contrast. In addition, we anticipated that averaging a large number of images would reduce possible bias introduced when particles with undetected distortions are included in the reconstruction.

The SV40 Capsid Structure. The two independent reconstructions revealed a nearly identical capsid structure. Fig. 2 shows a reconstruction based on the entire set of 30 particle images. The results demonstrate that both the pentavalent and hexavalent capsomeres of SV40 consist of pentameric substructures, indicating that the bonding specificity in the virion capsid is not quasi-equivalent.

The size and mass of the two types of capsomeres are approximately equal, as might be expected for pentameric oligomers composed of a single protein (VP1). The nearly identical organization of the capsid subunits found for both SV40 (shown here) and polyoma (7) may be a characteristic feature of all members of the papova family.

The outer surfaces of both types of capsomeres found on the SV40 virion capsid contain depressions ≈1.5 nm deep,

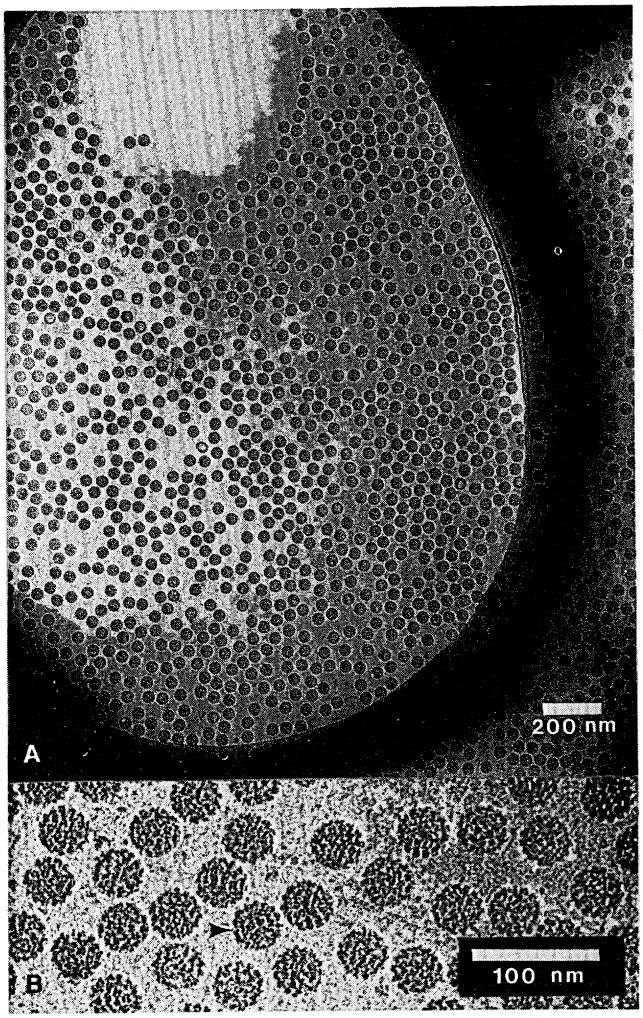

FIG. 1. (*A*) Low-magnification view of a frozen hydrated SV40 sample. Micrographs were recorded under low-irradiation conditions to minimize radiation-induced damage to the samples (29, 30). Individual virus particles are suspended over a hole in the carbon substrate within a thin layer of vitreous ice about the same thickness (≈50 nm) as the particle diameter. Particle contrast is significantly reduced in regions where the ice is too thick (>100 nm; not shown). The clear circular region, devoid of particles, presumably arises from an aqueous layer from which particles have migrated due to surface tension forces present when the layer becomes too thin to support the particles. Relative mass thickness measurements of different regions of the vitreous ice substantiate this hypothesis. The image was recorded 4–5 μm under focus to enhance phase contrast and accentuate the visibility of particle substructure at low magnification. (*B*) High-magnification image of a different region than shown in *A* of the vitrified SV40 sample, photographed 1–2 μm under focus. The contrast in the original micrograph has been enhanced to better visualize the capsomeres as well as the random orientation of the particles. Particle images from this micrograph were used to reconstruct the final three-dimensional structure. Arrow identifies a virus particle viewed close to a 3-fold symmetry axis.

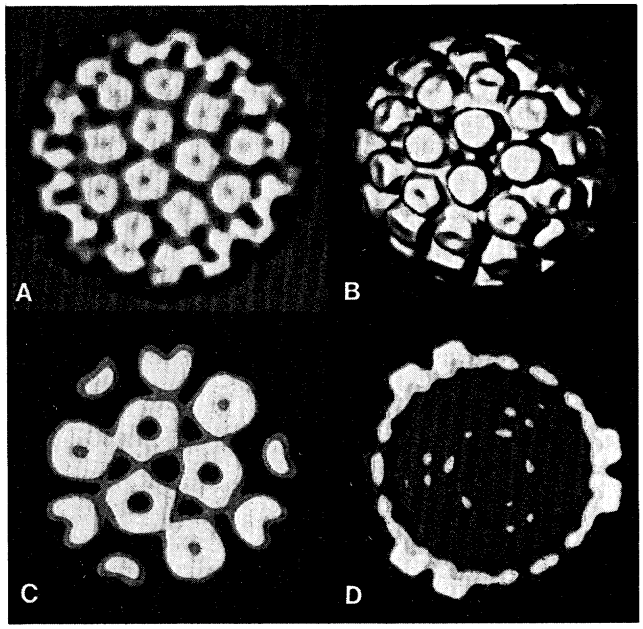

FIG. 2. The three-dimensional electron density reconstruction of SV40 viewed along a 3-fold icosahedral axis. Perfect 3-fold symmetry has not been imposed on the reconstruction; therefore, similarity of 3-fold related features in the displays is a measure of the preservation of icosahedral symmetry in the particles averaged. (*A*) Projection of one-half of the reconstruction viewed from the outside. Highest intensities in the display correspond to the features in the map with highest density (i.e., the reverse contrast of Fig. 1). (*B*) Solid-model surface-shaded representation of the density in *A*. This view reveals the prominent dimpled cap regions of the capsomeres and holes in the underlying shell region of the capsid. (*C*) Projected density corresponding to the shell region (between 1.84 and 2.03 nm, at the 3-fold axis). The pentameric substructure of the hexavalent capsomeres is clearly evident even though the axes of the capsomeres do not precisely coincide with the view direction. (*D*) Central section showing a cross-sectional profile of the hexavalent capsomeres, the weak density between the chromatin core and the inner boundary of the protein shell, and the density corresponding to the nucleohistone core. Absolute differences in density between the capsid and core regions of the virion may not be accurately represented in this reconstruction due to effects of the phase-contrast transfer function of the electron microscope. In addition, since the nucleohistone core is not organized with icosahedral symmetry, the core density is smeared by the averaging procedures and thus appears weaker than expected.

which appear as dimples (Fig. 2*B*). However, the pentavalent and hexavalent capsomeres are distinguishable when viewed from the inside (Fig. 3*C*). Whereas the inner surface of the hexavalent pentamers contains a prominent cavity, weak density extends along the axes of the pentavalent pentamers and merges with density in the chromatin core (Fig. 3). This density may correspond to the minor virion proteins (VP2, VP3) or represent an extended domain of VP1 contacting the nucleohistone core. At this resolution, these possibilities cannot be distinguished.

Distinct regions are observed in the capsid three-dimensional reconstruction: prominent protruding cylindrical regions (caps) and an underlying shell (Fig. 2 *B* and *D*). This suggests that protein subunits used in constructing the capsid may contain two distinct structural domains, possibly similar to the domains present in the tomato bushy stunt virus subunits (37). Association of five protruding domains could form the dimpled cylindrical caps, which extend radially from about 20.5 nm to 24.5 nm (Fig. 2 *B* and *D*).

At low radii in the capsid (18–20 nm), density is mainly contained in a thin shell, which appears to provide a supporting network that holds the projecting caps in place. Prominent holes are present in the shell regions where neighboring capsomeres do not appear to be in contact. For example, holes 2.5–3.0 nm in diameter are surrounded by the three capsomeres adjacent to each icosahedral 3-fold axis (Figs. 2 and 3*C*). Such holes may allow solvent, ions, and other small molecules to gain access to the virion interior. These holes may account for the finding that micrococcal nuclease can penetrate virions treated with a low concentration of dithiothreitol (38).

Inspection of sections through the electron density map at low radii (18–20.5 nm), in the basal portion of the capsid,

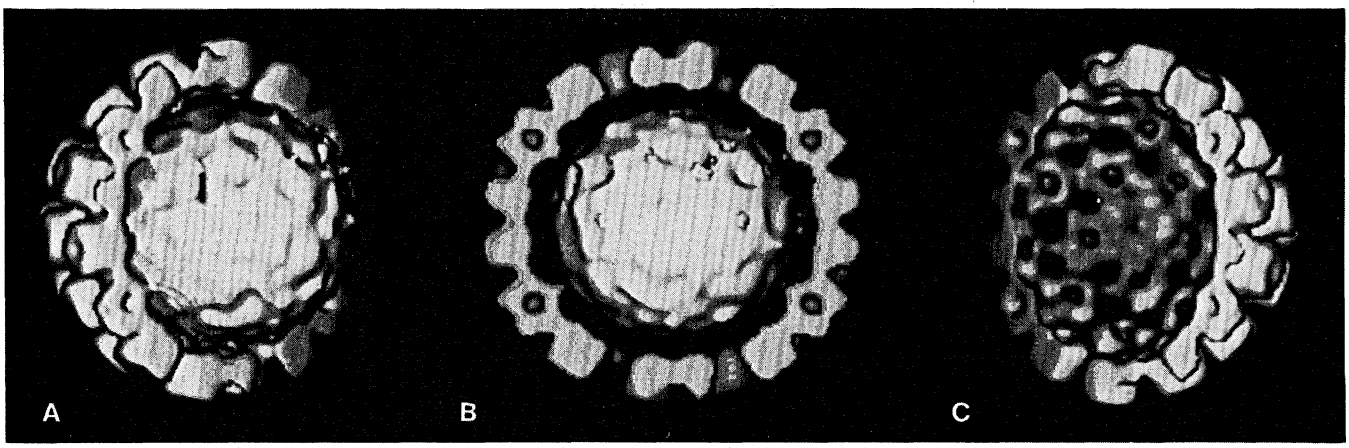

FIG. 3. Solid-model surface-shaded views of the SV40 virion, with half of the protein shell removed (*A* and *B*) to reveal the structure of the chromatin core and its interaction with the capsid. The surface-density value, which reflects "light" in these representations, was adjusted until the solid volume in the capsid corresponded to the expected volume occupied by 360 subunits of VP1. (*C*) The inner surface of the protein shell is exposed to reveal the presence of holes (see also Fig. 2*B*), depressions in the base of the hexavalent capsomeres, and density extending from the base of the pentavalent capsomeres toward the core (also *A* and *B*). Even though the reconstruction was not computed using icosahedral averaging (see *Materials and Methods* for details), all the pentavalent capsomeres appear similar and all the hexavalent capsomeres appear similar.

shows that the shell domains splay out in a tangential direction, forming the intersubunit contacts that may be mainly responsible for stabilizing the entire capsid structure. The inner surface of the capsid forms a nearly spherical boundary for the minichromosome in the interior of the virus (Figs. 2*D* and 3).

The Structure of Chromatin within the Core. A slice made through the center of the SV40 reconstruction shows the inner density corresponding to the chromatin core. A clear break (0.5–1.5 nm thick) separates density in the inner part of the capsid from density in the core (Figs. 2*D* and 3 *A* and *B*). The presence of a clear partition between the shell and chromatin is somewhat surprising because both biochemical and morphological studies have shown that the virion proteins (VP1, VP2, VP3) intimately interact with the minichromosome during SV40 assembly (39, 40). It is known, for example, that the virion proteins polymerize around the chromatin during the shell propagation step (1, 2, 39, 40), and that VP1 plays a key role in changing the spacing between nucleosomes during the initial stages of SV40 assembly (41, 42). The existence of strong interactions between the capsid and chromatin core at a limited number of specific sites is not ruled out by the electron density map; such contacts, if they do exist, would appear weaker after the averaging procedure. Moreover, flexibility or disorder in the chromatin-binding domains of the capsid proteins, as observed for example for the extended arm of the tomato bushy stunt virus capsid subunits (37), would cause the density between the capsid shell and the chromatin core to become smeared.

To learn about the specific organization of the minichromosome inside the virus (43–46), we have closely examined the distribution of densities within the core in the two independent image reconstructions. We observe that the density distribution in the region corresponding to the nucleohistone core does not exhibit reproducible features, whereas the strong features in the capsid portion are clearly apparent and are virtually identical in the two reconstructions. Since weak features in the core region have only ≈20% of the maximum contrast seen in the capsid (Fig. 2*D*) and are not identical in the two maps, it is likely that they arise from residual noise in the reconstruction. These observations clearly indicate that the minichromosome higher-order structure is not organized with an icosahedral symmetry that matches the symmetry of the capsid. This finding does not rule out the possibility of some symmetrical or ordered arrangement for the minichromosome.

The nucleohistone core must exist in a highly condensed state in the virion since it fits into an approximately spherical space with a volume of $\approx 2 \times 10^4$ nm^3. This volume was calculated from the radius of the sphere (16.5–17 nm) that delimits the chromatin density (e.g., see Fig. 2*D*). How nucleosomes are arranged within this volume remains a puzzle. We could estimate the maximum volume occupied by each nucleosome, if the exact number of nucleosomes present in the virions were known. Earlier studies indicated that the unencapsidated 75S chromatin contains ≈21 nucleosomes (47–49). However, the results of two independent recent studies show that the mean number of nucleosomes is ≈26 (50, 51). The heterogeneity in the number of nucleosomes is about ±4 (51). Thus, the average volume occupied by each nucleosome is ≈760 nm^3 (2×10^4 nm^3 per 26 nucleosomes). It is unlikely that the virion can accommodate more than 32 nucleosomes since there is suggestive evidence (52) that the minichromosomes assembled from DNA molecules whose lengths exceed the length of SV40 DNA by ≈10% are not encapsidated. A minichromosome core with 32 nucleosomes would place an upper limit on the smallest volume a nucleosome can occupy: 615 nm^3 (2×10^4 nm^3 per 32 nucleosomes). The estimated volumes do not take into account the volume occupied by other proteins (i.e., VP2 and VP3) or constraints imposed on the volume by the native structure and the nucleosome packing arrangement.

The SV40 reconstruction provides a basis for invoking additional models for the higher-order minichromosome structure. Such models ought to account for the volume and precise structure of nucleosomes and the topological changes imposed on the DNA during virion assembly (51, 53). The problem of determining the structure of chromatin within the virion core remains an exciting challenge.

We thank P. N. T. Unwin and colleagues for their advice, guidance, and patience in teaching and assisting with cryomicroscopy techniques and for the use of the Stanford Cell Biology Department Philips EM400 electron microscope and Gatan cold holder; N. Olson for photography, particle size measurements, and insightful comments; D. L. D. Caspar, D. J. DeRosier, G. Sosinsky, and W. T. Murakami (Brandeis University), and I. Rayment (University of Arizona) for advice and inspiration; L. A. Amos and R. A. Crowther (Molecular Research Council Laboratory of Molecular Biology, Cambridge, England) and S. Fuller (European Molecular Biology

Laboratory, Heidelberg) for icosahedral image processing programs; and M. Radermacker (New York State Department of Health) and C. Ho for surface shading algorithms. The work was supported by research grants awarded to T.S.B. (National Institutes of Health, the Showalter Fund, the Indiana Elks, the American Cancer Society, and start-up funds from Purdue University Department of Biological Sciences) and to M.B. (National Science Foundation and the American Cancer Society).

1. Bina, M., Ng, S.-C. & Blasquez, V. (1983) *J. Biomol. Struct. Dyn.* **1,** 689–704.
2. Bina, M. (1986) *Comments Mol. Cell. Biophys.* **4,** 55–62.
3. Tooze, J., ed. (1981) *Molecular Biology of Tumor Viruses*, DNA Tumor Viruses (Cold Spring Harbor Laboratory, Cold Spring Harbor, NY), Part 2.
4. Anderer, F. A., Schlumberger, H. D., Koch, M. A., Frank, H. & Eggers, H. J. (1967) *Virology* **32,** 511–523.
5. Koch, M. A., Eggers, H. J., Anderer, F. A., Schlumberger, H. D. & Frank, H. (1967) *Virology* **32,** 503–510.
6. Mayor, H. D., Jamison, R. M. & Jordan, L. E. (1963) *Virology* **19,** 359–366.
7. Rayment, I., Baker, T. S., Caspar, D. L. D. & Murakami, W. T. (1982) *Nature (London)* **295,** 110–115.
8. Caspar, D. L. D. & Klug, A. (1962) *Cold Spring Harbor Symp. Quant. Biol.* **27,** 1–24.
9. Baker, T. S., Caspar, D. L. D. & Murakami, W. T. (1983) *Nature (London)* **303,** 446–448.
10. Salunke, D. M., Caspar, D. L. D. & Garcea, R. L. (1986) *Cell* **46,** 895–904.
11. Taylor, K. A. & Glaeser, R. M. J. (1976) *Ultrastruct. Res.* **55,** 448–456.
12. Taylor, K. A. (1978) *J. Microsc. (Oxford)* **112,** 115–125.
13. Lepault, J., Booy, F. P. & Dubochet, J. (1983) *J. Microsc. (Oxford)* **129,** 89–102.
14. Milligan, R. A., Brisson, A. & Unwin, P. N. T. (1984) *Ultramicroscopy* **13,** 1–10.
15. Adrian, M., Dubochet, J., Lepault, J. & McDowall, A. W. (1984) *Nature (London)* **308,** 32–36.
16. Chiu, W. (1986) *Annu. Rev. Biophys. Biophys. Chem.* **15,** 237–257.
17. Stewart, M. & Vigers, G. (1986) *Nature (London)* **319,** 631–636.
18. Crowther, R. A., Amos, L. A., Finch, J. T., DeRosier, D. J. & Klug, A. (1970) *Nature (London)* **226,** 421–425.
19. Crowther, R. A., DeRosier, D. J. & Klug, A. (1970) *Proc. R. Soc. London Ser. A* **317,** 319–340.
20. Crowther, R. A. (1971) *Phil. Trans. R. Soc. London Ser. B* **261,** 221–230.
21. Baker, T. S. (1981) *Electron Microsc. Biol.* **1,** 189–290.
22. Friedmann, T. & Haas, M. (1970) *Virology* **42,** 248–250.
23. Bina, M., Beecher, S. & Blasquez, V. (1982) *Biochemistry* **21,** 3057–3063.
24. Erickson, H. P. & Klug, A. (1971) *Phil. Trans. R. Soc. London Ser. B* **261,** 105–118.
25. Lepault, J. & Leonard, K. (1985) *J. Mol. Biol.* **182,** 431–441.
26. DeRosier, D. J. & Moore, P. B. (1970) *J. Mol. Biol.* **52,** 355–369.
27. Fuller, S. D. (1987) *Cell* **48,** 923–934.
28. Klug, A. & Finch, J. T. (1968) *J. Mol. Biol.* **31,** 1–12.
29. Williams, R. C. & Fisher, H. W. (1970) *J. Mol. Biol.* **52,** 121–123.
30. Baker, T. S. & Amos, L. A. (1978) *J. Mol. Biol.* **123,** 89–106.
31. Crowther, R. A. & Amos, L. A. (1972) *Cold Spring Harbor Symp. Quant. Biol.* **36,** 489–494.
32. Mellema, J. E. & Amos, L. A. (1972) *J. Mol. Biol.* **72,** 819–822.
33. Crowther, R. A., Geelen, J. L. M. C. & Mellema, J. E. (1974) *Virology* **57,** 20–27.
34. Finch, J. T., Crowther, R. A., Henry, D. A. & Struthers, J. K. (1974) *J. Gen. Virol.* **24,** 191–200.
35. Crowther, R. A., Amos, L. A. & Finch, J. T. (1975) *J. Mol. Biol.* **98,** 631–635.
36. Finch, J. T. (1974) *J. Gen. Virol.* **24,** 359–364.
37. Harrison, S. C., Olson, A. J., Schutt, C. E., Winkler, F. K. & Bricogne, G. (1978) *Nature (London)* **276,** 368–373.
38. Ng, S.-C. & Bina, M. (1981) *FEBS Lett.* **30,** 47–49.
39. Blasquez, V., Beecher, S. & Bina, M. (1983) *J. Biol. Chem.* **258,** 8477–8484.
40. Ng, S.-C. & Bina, M. (1984) *J. Virol.* **50,** 471–477.
41. Blasquez, V., Stein, A., Ambrose, C. & Bina, M. (1986) *J. Mol. Biol.* **191,** 97–106.
42. Coca-Prados, M., Yu, H. & Hsu, M. T. (1982) *J. Virol.* **44,** 603–609.
43. Martin, R. G. (1977) *Virology* **83,** 433–437.
44. Varshavsky, A. J., Bakayev, V. V., Nedospasov, S. A. & Georgiev, G. P. (1978) *Cold Spring Harbor Symp. Quant. Biol.* **42,** 457–473.
45. Müller, U., Zetgraf, H., Eicken, I. & Keller, W. (1978) *Science* **201,** 406–415.
46. Dubochet, J., Adrian, M., Schultz, P. & Oudet, P. (1986) *EMBO J.* **5,** 519–528.
47. Griffith, J. D. (1975) *Science* **187,** 1202–1203.
48. Saragosti, S., Moyne, G. & Yaniv, M. (1980) *Cell* **20,** 65–73.
49. Jakobovitz, E. J., Bratsin, S. & Aloni, Y. (1980) *Nature (London)* **285,** 263–265.
50. Ambrose, C., McLaughlin, R. & Bina, M. (1987) *Nucleic Acids Res.* **15,** 3703–3721.
51. Sogo, J. M., Stahl, H., Koller, T. & Knippers, R. (1986) *J. Mol. Biol.* **189,** 189–204.
52. Chang, X.-B. & Wilson, J. H. (1986) *J. Virol.* **58,** 393–401.
53. Chen, S. S. & Hsu, M.-T. (1984) *J. Virol.* **51,** 14–19.